

The Impact of Tilt Grain Boundaries on the Thermal Transport in Perovskite SrTiO₃ Layered Nanostructures. A Computational Study.

Stephen R. Yeandel^{a,b}, Marco Molinari^{a,c}, Stephen C. Parker^{a,*}

^a Department of Chemistry, University of Bath, Claverton Down, Bath, BA2 7AY, U.K.

^b Department of Chemistry, Loughborough University, Epinal Way, Loughborough, LE11 3TU, U.K.

^c Department of Chemistry, University of Huddersfield, Queensgate, Huddersfield, HD1 3DH, U.K.

*E-mail: s.c.parker@bath.ac.uk and m.molinari@hud.ac.uk

Supporting Information

Table S1. Lattice parameters of the simulation cells for the 10nm-GB, 2nm-GB, and lattice dynamics (LD-GB) layered nanostructures separated by tilt grain boundaries. The a, b and c cell dimensions correspond to the direction x, y and z respectively.

System	a x b x c (nm)	$\alpha = \beta = \gamma$ (degree)
10nm-GB $\Sigma 3\{111\}/[\bar{1}10]$	20.3 x 2.2 x 1.9	90
10nm-GB $\Sigma 3\{112\}/[\bar{1}10]$	19.3 x 2.2 x 2.0	90
10nm-GB $\Sigma 5\{310\}/[001]$	19.9 x 2.0 x 3.7	90
2nm-GB $\Sigma 3\{111\}/[\bar{1}10]$	2.7 x 2.2 x 1.9	90
2nm-GB $\Sigma 3\{112\}/[\bar{1}10]$	3.9 x 2.2 x 2.0	90
2nm-GB $\Sigma 5\{310\}/[001]$	2.6 x 1.9 x 3.7	90
LD-GB $\Sigma 3\{111\}/[\bar{1}10]$	2.7 x 0.6 x 1.0	90
LD-GB $\Sigma 3\{112\}/[\bar{1}10]$	3.9 x 0.6 x 0.7	90
LD-GB $\Sigma 5\{310\}/[001]$	2.6 x 0.4 x 1.2	90

Section S1. Calculation of the heat flux and thermal conductivity

We used the Green-Kubo method^{1,2} as implemented in LAMMPS.³ First the heat-flux of the system is calculated using:

$$\mathbf{J} = \left[\sum_i e_i \mathbf{v}_i - \sum_i \mathbf{S}_i \mathbf{v}_i \right]$$

where \mathbf{J} is the heat-flux, e_i is the energy of atom i , \mathbf{v}_i is the velocity vector for atom i and \mathbf{S}_i is the stress tensor. This may also be expanded to give:

$$\mathbf{J} = \left[\sum_i e_i \mathbf{v}_i - \sum_{i < j} (\mathbf{f}_{ij} \cdot \mathbf{v}_j) \mathbf{r}_{ij} \right]$$

and further:

$$\mathbf{J} = \left[\sum_i e_i \mathbf{v}_i - \frac{1}{2} \sum_{i < j} (\mathbf{f}_{ij} \cdot (\mathbf{v}_i + \mathbf{v}_j)) \mathbf{r}_{ij} \right]$$

where \mathbf{f}_{ij} represents the force and \mathbf{r}_{ij} the separation between atoms i and j .

We have implemented a simple program to compute the autocorrelation of the heat-flux and then to integrate it, yielding a value proportional to the thermal conductivity:

$$\kappa = \frac{s \Delta t}{V k_B T^2} \int_0^\infty \langle \mathbf{J}(0) \cdot \mathbf{J}(t) \rangle \Delta t$$

where s is the integer number of steps between heat-flux sampling, Δt is the timestep of the simulation, V is the volume of the system, k_B is Boltzmann's constant and T is the temperature of the system.

To achieve a complete accounting of the heat flux, we have used the method of Sirk *et al.*⁴ (where a cubic 40Å simulation box of 2180 water molecules was deemed sufficient to avoid dependence on box length) of including a k-space contribution to the energy and virial, which is developed as an extension of particle-particle particle-mesh technique (PPPM).

Convergence test. The Green-Kubo method has been used in these calculations as convergence with respect to system size is reached relatively quickly compared to NEMD⁵ as finite size effects are much reduced by the absence of a heat source/sink. Additionally, data for independent dimensions of a system can be obtained simultaneously during a single simulation using the Green-Kubo method. A final consideration is that in calculations using the Green-Kubo method there is no heat source/sink and so its placement relative to the grain boundary and the difficulty of extrapolating to infinite length in NEMD calculations is avoided.⁵

We have performed convergence tests on the 2nm-GB $\Sigma 3\{111\}/[\bar{1}10]$. We have calculated the thermal conductivity and the heat-flux autocorrelation function (HFACF) spectra for a $1 \times 2 \times 2$ expansion of the 2nm-GB $\Sigma 3\{111\}/[\bar{1}10]$ (Table S1 present the $1 \times 1 \times 1$ unit cell). The thermal conductivity of a $1 \times 1 \times 1$ and of the $1 \times 2 \times 2$ unit cells are all within the fluctuation bounds. Figure S1 presents the comparison. Fluctuation bounds for calculations using the Green-Kubo method can be very large, greater than 20% even in well converged data as demonstrated by Schelling *et al.*⁵ Additionally, specifying the point at which the Green-Kubo integral has converged can be extremely challenging as stated by McGaughey and Larkin.⁶ We have used the bottle-neck regime to calculate the fluctuation bounds as explained by McGaughey and Kaviany.⁷ This is currently the only way available to do so using the Green-Kubo method to calculate fluctuation bounds of thermal conductivity values.

The size of the simulation cell imparts periodic constraint on how atoms may vibrate and that other atoms may display spurious correlations due to the periodic images, but this effect is minimised by two key factors: (1) the thermal conductivity of bulk SrTiO₃ is converged with respect to simulation cell size, indicating spurious vibrational correlations are negligible in bulk SrTiO₃ at this size, and (2) the scattering in the grain boundary systems is significantly increased compared to the bulk material due to the presence of grain boundaries and thus the phonon mean free path is reduced, allowing a smaller simulation size than is needed for a pure bulk material.⁶

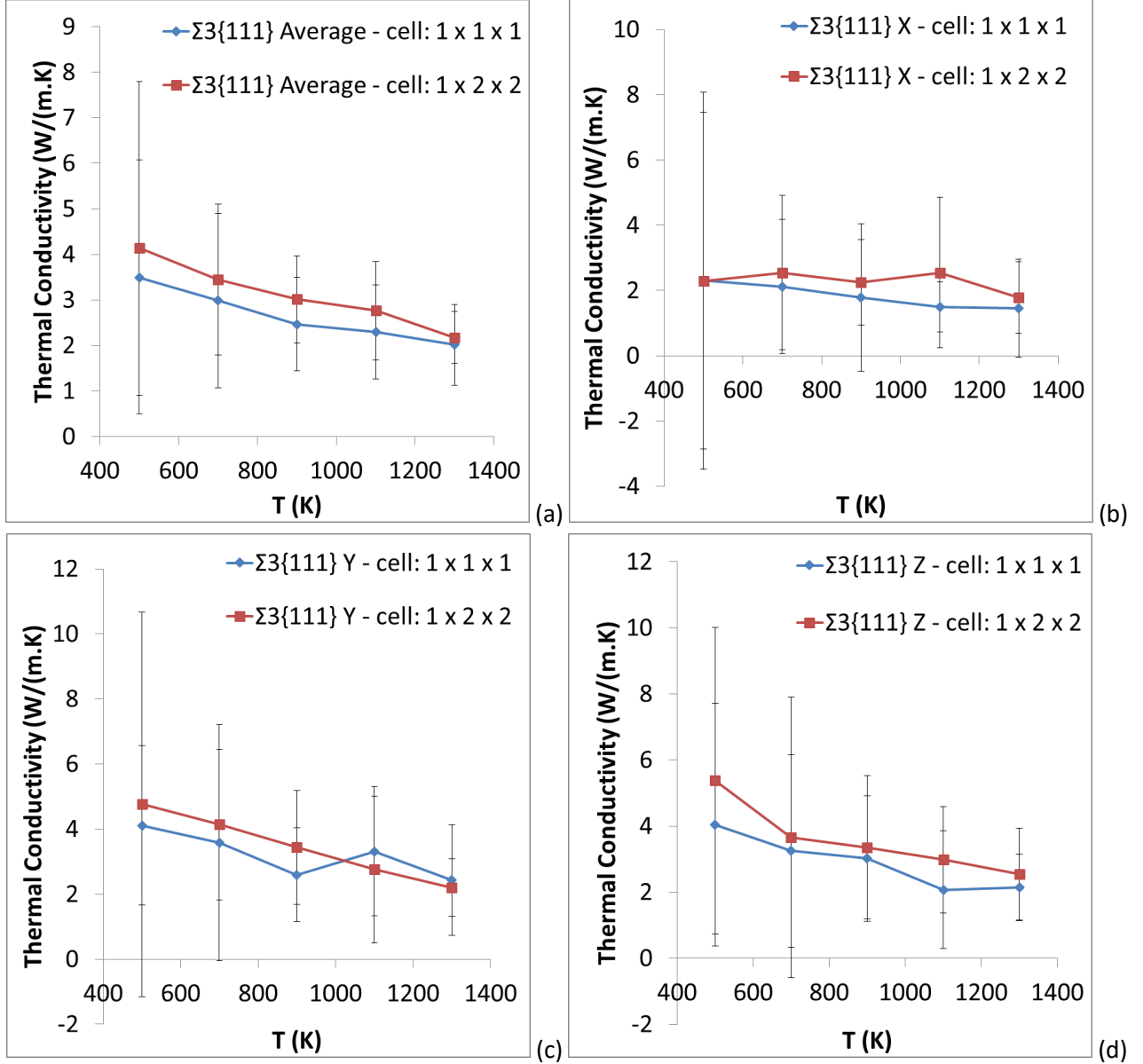


Figure S1. (a) Average, (b) x, (c) y and (d) z components of the thermal conductivity for a 1x1x1 and 1x2x2 unit cell of the 2nm-GB $\Sigma 3\{111\}/[\bar{1}10]$ grain boundary.

To support that our values for the thermal conductivity are also converged, one can think about the mean free path of phonons. Calculation of mean-free-path is performed by using a simple kinetic approximation as explained by Dove:⁸

$$\kappa = \frac{1}{3} C_V \langle v \rangle L$$

This expression may be rearranged to give the phonon mean-free-path, L . The thermal conductivity, κ , is calculated via molecular dynamics calculations of bulk SrTiO₃ using the LAMMPS code.³ A thermal conductivity value of 8 W/(m.K) at 500 K was obtained.⁹ The heat capacity per unit volume, C_V , and the average speed of the phonons, $\langle v \rangle$, are calculated from lattice dynamics calculations as implemented in the GULP code.¹⁰ All properties were calculated using the Teter potential model¹¹ and an energy minimised unit cell of stoichiometric bulk SrTiO₃. The heat capacity per unit volume for bulk SrTiO₃ is calculated to be 3,085,136 J/(K.m³). Lattice dynamics calculations also yield the velocities of two types of phonons, S-

waves (V_S , transverse, 4,822 m/s) and P-waves (V_P , longitudinal, 8,352 m/s) computed from the bulk (G) and shear modulus (K) of the material along with the density (ρ):

$$V_S = \sqrt{\frac{G}{\rho}}$$

$$V_P = \sqrt{\frac{4G + 3K}{3\rho}}$$

Using these values the faster P-waves indicate a phonon mean-free-path in bulk SrTiO₃ of ~9.3 Å and the slower S-waves give a value of ~16.1 Å. Both of these values calculated for bulk SrTiO₃ are shorter than the size of all our simulation cells (in all directions) (Table S1) used for calculation of thermal conductivity in our layered nanostructures.

Section S2. Identification of peaks in the heat-flux autocorrelation function (HFACF) spectra

Models. To analyse the contribution of each vibrational mode to the total heat-flux from the different regions (i.e. grain boundary and inter-boundary regions) of our simulated systems (i.e. layered nanostructures separated by tilt grain boundaries), it is first necessary to define the regions within the system that contribute to the “Grain Boundary” and to the “Inter-Boundary”, referred to as GB and IB, respectively. The three layered nanostructures containing the $\Sigma 3\{111\}/[\bar{1}10]$, $\Sigma 3\{112\}/[\bar{1}10]$ and $\Sigma 5\{310\}/[001]$ grain boundaries respectively are constructed so that these two regions (i.e. GB and IB) have the same number of atoms. The IB and GB regions are structurally different. All species in the IB regions have local coordination environments for Sr, Ti and O species that are the same as in bulk SrTiO₃, whereas in the GB regions, Sr, Ti and O species have different coordination environments compared to bulk SrTiO₃ because of the presence of the extended defect. The dimensions of the simulation cells for these models (LD-GB) are in Table S1. There are two of each region in the layered nanostructures, due to the way we construct the configurations.¹² This is shown in Figure S2 for the layered nanostructure containing the $\Sigma 3\{111\}/[\bar{1}10]$ grain boundary. We have imposed an additional constraint on the definition of the regions so that it must be possible to construct a single crystal SrTiO₃ using only the inter-boundary regions IB_A or IB_B. Thus, by taking either region IB_A or IB_B alone, it is possible to reconstruct a bulk SrTiO₃ system orientated in the [111] direction.

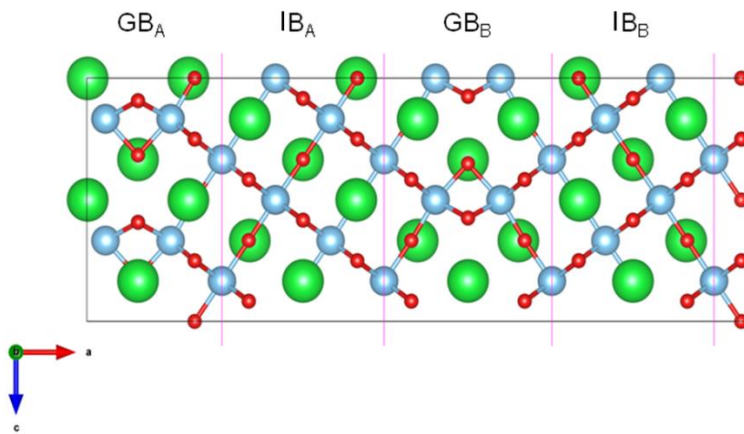


Figure S2. Schematic representation of the regions within the layered nanostructure containing the $\Sigma 3\{111\}/[\bar{1}10]$ grain boundary. There are two grain boundaries running in opposite directions labelled as GB_A and GB_B equally spaced by two inter-boundary regions labelled as IB_A and IB_B.

Methodology. To analyse the contribution of the different regions, GB and IB, on the scattering effect of the different vibrational modes, first the Γ -point vibrational modes are calculated along with their corresponding eigenvectors using the METADISE¹³ and the Phonopy¹⁴⁻¹⁶ codes. The eigenvectors for each vibrational mode given by Phonopy are then summed in each dimension (i.e. x, y and z). Modes with an eigenvector sum below a small cutoff of intensity 0.01 a.u. are not included in our analysis in order to avoid background noise. This enables us to generate the phonon density of state (PDOS) for the three x, y and z dimensions separately, expressing only the vibrational mode with non-zero sum of the eigenvectors. In our previous work,⁹ we have demonstrated that this procedure allows us to compare the PDOS calculated using lattice dynamics with the spectrum of the heat-flux autocorrelation function (HFACF) derived from molecular dynamics calculations. The vibrational modes with an eigenvector sum of zero in all three dimensions will not appear in the spectrum of the heat-flux autocorrelation function. This is because all vibrational motions are exactly cancelled by an anti-symmetric motion of

a symmetry equivalent atom elsewhere in the system. Therefore in these vibrational modes the centre of mass of the system does not change (zero momentum), and additionally there cannot be net heat-flux during the vibration as the energy moving in a given direction is exactly cancelled by energy moving in the opposite direction. These vibrational modes are “Inactive Modes”.

When the sum of eigenvectors is non-zero, there is no exact cancellation of vibrational motions over the entire system. While the momentum of the simulated system is still zero, there is now a disparity in the number of species moving in a given direction at any given time. This disparity gives rise to a net system heat-flux oscillating in a specific direction over time. These vibrational modes are “Active Modes”.

A rigorous mathematical derivation of this principle is given in the appendix of Landry et al.¹⁷

Figure S3 shows the phonon density of states at the Γ -point before and after removing the inactive modes for stoichiometric bulk SrTiO_3 (i.e. equivalent to a stoichiometric infinite single crystal). Figure S3a shows the PDOS with four Longitudinal Optical (LO) Modes at 5.7 THz, 11.0 THz, 14.1 THz and 22.4 THz. One mode is removed as its eigenvector sum is equal to zero, and therefore the mode will not be associated with either a net change in heat-flux or in dipole moment (IR inactive mode). Figure S3b shows the PDOS containing only active modes. Gaussian functions are used to represent the modes. The magnitude of the Gaussian functions are set to the absolute value of the eigenvector sum for the mode and serves only as a guide to the eye for comparison with the HFACF spectra. An arbitrary broadening parameter of 0.1 THz is used for all Gaussians. Thus it becomes clear that the peaks at 5.7 THz, 14.1 THz and 22.4 THz are active modes whereas the peak at 11.0 THz is an inactive mode.

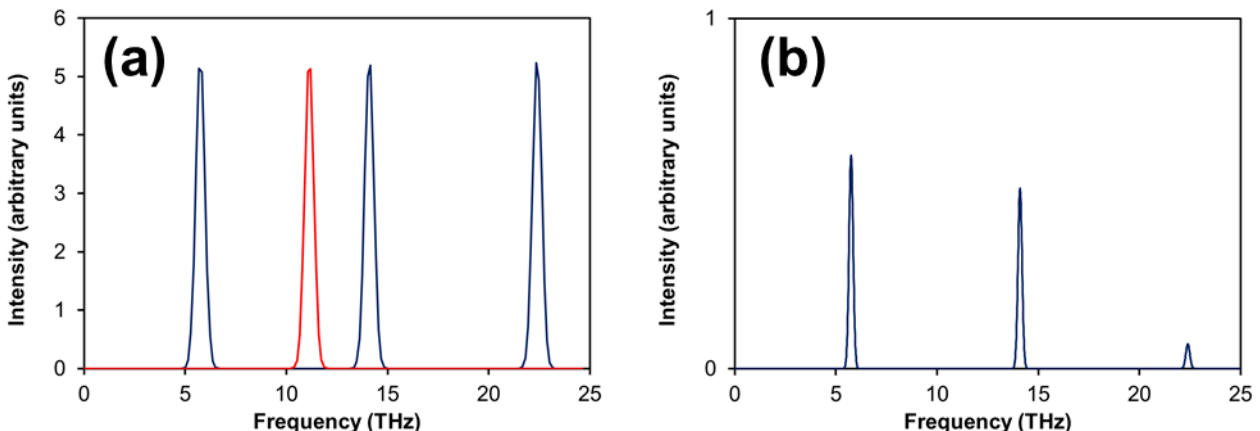


Figure S3. PDOS at the gamma point for stoichiometric bulk SrTiO_3 , (a) containing all active (blue) and inactive (red) vibrational modes, and (b) containing only active vibrational modes.

In order to provide some statistical analysis of the nature of the vibrational modes in the layered nanostructures, we have devised analyses that can divide the vibrational modes depending on whether they have a predominant character arising from the IB or GB regions, referred as “Per-Region Analysis”, whether they have an in-plane (parallel to the grain boundary) or out-of-plane (perpendicular to the grain boundary) character, referred as “Per-Direction Analysis”, and whether they involved predominantly Sr, Ti or O species, referred as “Per-Species Analysis”. These analyses are based on Figure 5 in the main manuscript. All data is presented in Tables S1, S2 and S3 outline the frequency of each vibrational mode, the “Direction”, the “Region” and the “Species” for each layered nanostructures containing the $\Sigma 3\{111\}/[\bar{1}10]$, $\Sigma 3\{112\}/[\bar{1}10]$ and $\Sigma 5\{310\}/[001]$ grain boundary respectively.

First of all, discussion from this point onwards is concerned only with active modes shown in the HFACF spectra. However, these spectra are of difficult interpretation and thus why we have evaluated the Phonon Density of States (PDOS) using lattice dynamics calculations. As we mentioned above, lattice dynamics calculations provide both the eigenvalues (the vibrational frequencies, λ_i) and the associated eigenvectors to the vibrational frequency. These associated eigenvectors for a given vibrational frequency (eigenvalue, λ_i), can be seen as a $N \times 3$ matrix, \mathbf{A}_i , where N is the number of atoms in the system and 3 corresponds to the directions of the simulation cell x , y and z . The eigenvectors correspond physically to the motion of the atoms in the system associated to a particular vibrational mode, and thus the matrix is the collective vibrational motion of the entire structure.

By defining \mathbf{A}_i , the different components of the vibrational mode can be isolated. \mathbf{A}_i may be broken down in many ways but we have chosen the “Per-Region Analysis”, “Per-Direction Analysis”, and “Per-Species Analysis”.

The matrix \mathbf{A}_i takes the form:

$$\mathbf{A}_i = \begin{bmatrix} a_{i,1,x} & a_{i,1,y} & a_{i,1,z} \\ a_{i,2,x} & a_{i,2,y} & a_{i,2,z} \\ \vdots & \vdots & \vdots \\ a_{i,N,x} & a_{i,N,y} & a_{i,N,z} \end{bmatrix}$$

We can express \mathbf{A}_i in terms of a list of N vectors, each of length 3, corresponding to each atom in the system:

$$\mathbf{A}_i = \begin{bmatrix} \mathbf{a}_{i,1} \\ \vdots \\ \mathbf{a}_{i,N} \end{bmatrix}$$

where:

$$\mathbf{a}_{i,k} = [a_{i,k,x}, a_{i,k,y}, a_{i,k,z}]$$

Per-Direction Analysis The vector $\mathbf{a}_{i,k}$ represents the displacement of atom k in the x , y and z directions respectively. Summation over all atoms in the system yields a single length 3 vector, \mathbf{b}_i .

$$\mathbf{b}_i = [b_{i,x}, b_{i,y}, b_{i,z}] = \sum_{k=1}^N \mathbf{a}_{i,k}$$

If any component of \mathbf{b}_i is non-zero, then the corresponding frequency, λ_i , will appear in the spectrum of the HFACF. Using this approach a phonon density-of-states (PDOS) may be easily constructed from the lattice dynamics calculation, yielding direct correspondence to the spectrum of the HFACF.

The vibrational mode λ_i is thus assigned a directional component of either x , y or z depending on the maximum absolute component of \mathbf{b}_i . If $|b_{i,x}| > |b_{i,y}|, |b_{i,z}|$ then the vibration has a predominant direction in x , if $|b_{i,y}| > |b_{i,x}|, |b_{i,z}|$ then the vibration has a predominant direction in y , and if $|b_{i,z}| > |b_{i,x}|, |b_{i,y}|$ then the vibration has a predominant direction in z . This predominant direction component is expressed as x , y and z in the “direction” column of Tables S2-S4.

Figure 5a in the main manuscript is simply constructed by counting all vibrational frequencies λ_i that have a given directional component and expressing them as a percentage. The x direction is expressed as perpendicular (\perp), while the y and z directions are summed into the parallel component (\parallel). The parallel component (\parallel) has been normalised to account for the existence of two directions (the count is divided by two).

Per-Region Analysis. To evaluate the contributions of different regions, R , of the system, we first classify each atom as belonging to either the Inter-Boundary (IB) or Grain-Boundary (GB) region. The IB region is the region between two boundaries, whereas the GB region is the region comprising the grain boundary. The number of atoms in a region is denoted by N_R . For each vibrational frequency, a summation of the vectors $\mathbf{a}_{i,k}$ can be performed on the atoms N_R belonging to IB and GB regions separately.

$$\mathbf{b}_{i,R} = [b_{i,R,x}, b_{i,R,y}, b_{i,R,z}] = \sum_{k=1}^{N_R} \mathbf{a}_{i,k}$$

By calculating the magnitude of the vector $\mathbf{b}_{i,R}$ it is possible to define which region has the stronger contribution.

$$b_{i,R} = \|\mathbf{b}_{i,R}\|$$

This will define whichever contribution is greater, $b_{i,GB}$ or $b_{i,IB}$, which will determine whether the vibrational mode (λ_i) is classified as being dominant in the GB or IB region. Thus, for every vibrational frequency if $b_{i,GB} > b_{i,IB}$, the vibration has a predominant contribution from the grain boundary (GB), whereas if $b_{i,GB} < b_{i,IB}$, the vibration has a predominant contribution from the inter-boundary (IB) region. This classification can be found under “Region” in Tables S2-S4.

As before the number of vibrational modes of each character (GB and IB) are counted and expressed as a percentage, this represents the location contribution in Figure 5b in the main manuscript.

It must be noted that although the different characters may arise from the IB region, the vibrational mode may only occur due to the presence of the GB region. This is because of the presence of extended defects (i.e. grain boundaries) induce complex vibrational motions in the layered nanostructures. Our analysis is able to differentiate between vibrational modes active mainly in the grain boundary (GB) or the inter-boundary (IB) regions under the constraints of using equal numbers of atoms in the two regions and self-periodicity of the inter-boundary regions, as stated in the “model” section.

The sums of eigenvectors for the two regions (i.e. GB and IB) may also agree or disagree in their sign. We term this “directional agreement” and for each mode it is either “TRUE” (i.e. agree) or “FALSE” (i.e. disagree). We can also indicate the relative strength of the contribution of the different regions in terms of a simple ratio of the sums of the eigenvectors in each region (i.e. IB and GB) for the same vibrational mode, where the maximum value for the contribution is set to 1.0. For example, it can be seen in Table S1 that the two modes at 2.71 THz occur in the “direction” z and y , which are equivalent.

They are dominant in the inter-boundary region “IB” (set to +1.0), but the grain boundary region “GB” has a response nearly equal in magnitude in the opposite direction indicated by a negative sign (-0.975).

Per-Species Analysis. We can also extend the analysis of the vibrational modes by performing the summation of the eigenvectors $\mathbf{a}_{i,k}$ over the different species (i.e. Sr, Ti or O) in the system, rather than in regions. For each vibrational mode (λ_i) we can sum the eigenvectors of all Sr, or Ti or O species separately; we refer to the species with the index s . N_s is the total number of any of Sr, or Ti, or O in the entire structure.

$$\mathbf{b}_{i,s} = [b_{i,s,x}, b_{i,s,y}, b_{i,s,z}] = \sum_{k=1}^{N_s} \mathbf{a}_{i,k}$$

It is then possible to assign a vibration type (i.e. the species involved the most in the vibration Sr, Ti or O) to each vibrational mode λ_i . This is not as simple as calculating which species has the largest magnitude (i.e. contributes the most to the vibration), as this is influenced by the stoichiometry of the system. Instead, the value $b_{i,s,d}$ is extracted from $\mathbf{b}_{i,s}$, for each species, where d is the direction of the vibrational modes (whether x , y or z). For each species, the sign of $b_{i,s,d}$ indicates whether the atoms of that species are moving in the $+d$ or $-d$ direction on average. By comparing the signs of $b_{i,s,d}$ for all species at the same vibrational frequency, it is possible to group together species which on average move together. An example is provided. For a vibrational mode λ_i :

$$\begin{aligned}\mathbf{b}_{i,Sr} &= [0.0_{i,Sr,x}, 0.0_{i,Sr,y}, +0.14_{i,Sr,z}] \\ \mathbf{b}_{i,Ti} &= [0.0_{i,Ti,x}, 0.0_{i,Ti,y}, -0.10_{i,Ti,z}] \\ \mathbf{b}_{i,O} &= [0.0_{i,O,x}, 0.0_{i,O,y}, -0.14_{i,O,z}]\end{aligned}$$

And the overall system vector, \mathbf{b}_i , is calculated to be:

$$\mathbf{b}_i = [0.0_{i,x}, 0.0_{i,y}, -0.10_{i,z}]$$

The direction, d , is therefore assigned as:

$$d = z$$

as the component z is non-zero.

The directional components are then extracted according to d . Thus:

$$\begin{aligned}b_{i,Sr,z} &= +0.14 \\ b_{i,Ti,z} &= -0.10 \\ b_{i,O,z} &= -0.14\end{aligned}$$

From these values it is clear that, on average, Ti and O move together while Sr moves in the opposite direction. Thus this mode will be assigned as Sr/Ti-O in “Species” in Tables S2-S4. In this example, the Sr atoms move in the opposite direction to the Ti and O atoms, and so this may be considered akin to a “Sr rattling” type mode. However, the greatest contribution to the heat-flux is actually from the Ti-O framework. This can be rationalised in terms of the total momentum which must be zero for any vibrational mode. Therefore any “rattling” type vibration of an atom must be counterbalanced by the opposite movement of the Ti-O framework, ensuring zero momentum. As the Ti-O network has a larger number of atoms and the time average kinetic energy of atoms is equal irrespective of species, then it follows that the biggest contribution to the heat-flux is from the Ti-O network. As before the number of vibrational modes of each character (primary Sr, Ti or O character) are counted and expressed as a percentage. This represents the “Species” contribution in Figure 5c in the main manuscript.

Table S2. Index of the vibrational modes in $\Sigma 3\{111\}/[\bar{1}10]$

Frequency (THz)	Direction	Region	Directional Agreement	"GB" : "IB"	Species
2.71	z	IB	FALSE	-0.975 : 1	Sr/Ti-O
2.71	y	IB	FALSE	-0.975 : 1	Sr/Ti-O
3.21	x	IB	FALSE	-0.547 : 1	Sr/Ti-O
3.99	x	IB	FALSE	-0.694 : 1	Sr/Ti-O
4.15	y	GB	FALSE	1 : -0.563	Sr/Ti-O
4.15	z	GB	FALSE	1 : -0.562	Sr/Ti-O
4.41	z	IB	FALSE	-0.908 : 1	Sr/Ti-O
4.41	y	IB	FALSE	-0.908 : 1	Sr/Ti-O
4.55	x	GB	FALSE	1 : -0.579	Sr/Ti-O
4.65	y	IB	TRUE	0.067 : 1	Sr/Ti-O
4.65	z	IB	TRUE	0.067 : 1	Sr/Ti-O
5.39	x	GB	FALSE	1 : -0.066	Sr/Ti-O
5.39	x	GB	FALSE	1 : -0.068	Sr/Ti-O
5.53	y	GB	TRUE	1 : 0.568	Sr/Ti-O
5.53	z	GB	TRUE	1 : 0.568	Sr/Ti-O
6.44	y	IB	FALSE	-0.875 : 1	Sr/Ti-O
6.44	z	IB	FALSE	-0.875 : 1	Sr/Ti-O
7.62	x	IB	FALSE	-0.954 : 1	Sr/Ti-O
7.87	y	GB	FALSE	1 : -0.476	O/Sr-Ti
7.87	z	GB	FALSE	1 : -0.476	O/Sr-Ti
11.01	x	IB	FALSE	-0.192 : 1	O/Sr-Ti
11.02	z	GB	FALSE	1 : -0.517	Ti/Sr-O
11.02	y	GB	FALSE	1 : -0.515	Ti/Sr-O
11.93	y	GB	TRUE	1 : 0.362	Ti/Sr-O
11.93	z	GB	TRUE	1 : 0.366	Ti/Sr-O
13.64	y	IB	TRUE	0.001 : 1	O/Sr-Ti
13.64	z	IB	TRUE	0.002 : 1	O/Sr-Ti
14.09	x	IB	TRUE	0.946 : 1	Ti/Sr-O
14.18	x	IB	TRUE	0.975 : 1	Ti/Sr-O
14.23	y	IB	TRUE	0.359 : 1	Ti/Sr-O
14.23	z	IB	TRUE	0.359 : 1	Ti/Sr-O
15.31	z	GB	FALSE	1 : -0.222	Ti/Sr-O
15.31	y	GB	FALSE	1 : -0.222	Ti/Sr-O
16.32	y	GB	FALSE	1 : -0.818	Ti/Sr-O
16.32	z	GB	FALSE	1 : -0.819	Ti/Sr-O
18.22	y	GB	FALSE	1 : -0.699	Ti/Sr-O
18.22	z	GB	FALSE	1 : -0.699	Ti/Sr-O
18.88	x	GB	FALSE	1 : -0.98	Sr/Ti-O
18.91	y	IB	FALSE	-0.563 : 1	O/Sr-Ti

18.91	z	IB	FALSE	-0.563 : 1	O/Sr-Ti
19.92	x	IB	FALSE	-0.705 : 1	O/Sr-Ti
20.48	y	GB	FALSE	1 : -0.722	O/Sr-Ti
20.48	z	GB	FALSE	1 : -0.722	O/Sr-Ti
21.28	x	GB	FALSE	1 : -0.822	O/Sr-Ti
22.59	y	GB	TRUE	1 : 0.234	O/Sr-Ti
22.59	z	GB	TRUE	1 : 0.234	O/Sr-Ti
22.74	x	IB	FALSE	-0.783 : 1	Ti/Sr-O
25.85	x	GB	FALSE	1 : -0.302	Ti/Sr-O
27.87	x	GB	FALSE	1 : -0.897	O/Sr-Ti

Table S3. Index of the vibrational modes in $\Sigma 3\{112\}/[\bar{1}10]$

Frequency (THz)	Direction	Region	Directional Agreement	"GB" : "IB"	Species
0.56	x	GB	FALSE	1 : -0.184	Sr/Ti-O
1.82	z	GB	FALSE	1 : -0.888	Sr/Ti-O
2.14	x	IB	FALSE	-0.939 : 1	Sr/Ti-O
2.20	z	IB	FALSE	-0.994 : 1	Sr/Ti-O
2.31	y	IB	FALSE	-0.977 : 1	Sr/Ti-O
3.28	z	GB	FALSE	1 : -0.826	Sr/Ti-O
3.34	x	IB	FALSE	-0.655 : 1	Sr/Ti-O
3.43	y	GB	FALSE	1 : -0.503	Sr/Ti-O
3.52	x	IB	FALSE	-0.806 : 1	Sr/Ti-O
3.60	z	GB	FALSE	1 : -0.724	O/Sr-Ti
3.67	x	IB	FALSE	-0.818 : 1	Sr/Ti-O
3.84	y	GB	TRUE	1 : 0.262	Sr/Ti-O
3.91	z	GB	FALSE	1 : -0.905	Sr/Ti-O
3.93	x	GB	FALSE	1 : -0.93	Sr/Ti-O
3.96	y	IB	FALSE	-0.14 : 1	Sr/Ti-O
4.11	x	GB	FALSE	1 : -0.744	Sr/Ti-O
4.13	x	IB	FALSE	-0.902 : 1	Sr/Ti-O
4.14	z	GB	FALSE	1 : -0.683	Sr/Ti-O
4.23	y	IB	FALSE	-0.914 : 1	O/Sr-Ti
4.38	y	GB	FALSE	1 : -0.83	Sr/Ti-O
4.40	z	GB	FALSE	1 : -0.05	Sr/Ti-O
4.41	x	GB	TRUE	1 : 0.305	Sr/Ti-O
4.47	z	GB	FALSE	1 : -0.715	Sr/Ti-O
4.50	x	IB	FALSE	-0.866 : 1	Sr/Ti-O
4.52	z	GB	FALSE	1 : -0.771	Sr/Ti-O
4.84	x	GB	FALSE	1 : -0.515	Sr/Ti-O
4.90	y	GB	FALSE	1 : -0.153	Sr/Ti-O
5.05	z	GB	TRUE	1 : 0.097	Sr/Ti-O
5.36	x	GB	TRUE	1 : 0.371	Sr/Ti-O
5.37	y	GB	TRUE	1 : 0.196	Sr/Ti-O
5.69	x	GB	FALSE	1 : -0.067	Sr/Ti-O
5.74	z	IB	TRUE	0.186 : 1	Sr/Ti-O
5.80	y	IB	TRUE	0.944 : 1	Sr/Ti-O
5.86	z	IB	FALSE	-0.719 : 1	Sr/Ti-O
5.94	y	IB	FALSE	-0.134 : 1	Sr/Ti-O
6.25	y	IB	FALSE	-0.557 : 1	Sr/Ti-O
6.29	x	IB	FALSE	-0.358 : 1	Sr/Ti-O
6.31	z	GB	FALSE	1 : -0.235	Sr/Ti-O
6.52	y	GB	FALSE	1 : -0.283	Sr/Ti-O

6.66	x	IB	FALSE	-0.592 : 1	Sr/Ti-O
6.76	z	GB	FALSE	1 : -0.204	Sr/Ti-O
6.77	x	IB	FALSE	-0.334 : 1	Sr/Ti-O
6.99	y	GB	FALSE	1 : -0.943	Ti/Sr-O
7.16	y	GB	FALSE	1 : -0.823	Sr/Ti-O
7.17	z	GB	FALSE	1 : -0.85	Sr/Ti-O
7.26	z	GB	FALSE	1 : -0.729	Ti/Sr-O
7.53	x	IB	FALSE	-0.214 : 1	Sr/Ti-O
7.74	z	IB	FALSE	-0.737 : 1	Sr/Ti-O
7.83	x	GB	FALSE	1 : -0.517	Sr/Ti-O
8.00	y	GB	FALSE	1 : -0.871	Sr/Ti-O
8.27	z	GB	FALSE	1 : -0.672	Sr/Ti-O
8.51	x	GB	FALSE	1 : -0.671	Sr/Ti-O
9.05	y	GB	FALSE	1 : -0.096	O/Sr-Ti
9.08	x	GB	FALSE	1 : -0.523	Sr/Ti-O
9.27	z	GB	FALSE	1 : -0.071	O/Sr-Ti
9.65	x	IB	FALSE	-0.746 : 1	Ti/Sr-O
9.73	z	IB	FALSE	-0.918 : 1	Ti/Sr-O
9.88	y	GB	FALSE	1 : -0.603	O/Sr-Ti
10.19	z	GB	FALSE	1 : -0.699	O/Sr-Ti
10.21	x	IB	FALSE	-0.913 : 1	Ti/Sr-O
10.35	x	GB	FALSE	1 : -0.881	Ti/Sr-O
10.52	z	IB	FALSE	-0.559 : 1	O/Sr-Ti
10.93	y	GB	FALSE	1 : -0.643	Ti/Sr-O
11.03	y	GB	FALSE	1 : -0.19	O/Sr-Ti
11.29	x	IB	FALSE	-0.196 : 1	Sr/Ti-O
11.38	z	GB	TRUE	1 : 0.537	O/Sr-Ti
11.44	x	IB	FALSE	-0.39 : 1	Sr/Ti-O
11.48	z	IB	TRUE	0.544 : 1	Ti/Sr-O
11.59	y	IB	FALSE	-0.409 : 1	Ti/Sr-O
11.71	x	IB	FALSE	-0.826 : 1	Ti/Sr-O
11.73	z	GB	TRUE	1 : 0.048	Ti/Sr-O
11.78	y	GB	FALSE	1 : -0.554	O/Sr-Ti
11.92	y	IB	FALSE	-0.266 : 1	O/Sr-Ti
12.05	x	IB	FALSE	-0.53 : 1	Sr/Ti-O
12.06	z	GB	FALSE	1 : -0.607	Sr/Ti-O
12.30	y	GB	FALSE	1 : -0.625	Ti/Sr-O
12.33	z	IB	FALSE	-0.417 : 1	Ti/Sr-O
12.46	z	GB	FALSE	1 : -0.565	O/Sr-Ti
12.47	x	GB	FALSE	1 : -0.722	Sr/Ti-O
12.57	y	GB	FALSE	1 : -0.714	Ti/Sr-O

13.35	y	GB	FALSE	1 : -0.255	O/Sr-Ti
13.64	x	GB	TRUE	1 : 0.791	O/Sr-Ti
13.96	x	GB	TRUE	1 : 0.709	O/Sr-Ti
14.07	z	IB	TRUE	0.212 : 1	O/Sr-Ti
14.10	x	GB	TRUE	1 : 0.724	O/Sr-Ti
14.12	y	IB	TRUE	0.222 : 1	O/Sr-Ti
14.40	z	GB	FALSE	1 : -0.031	O/Sr-Ti
14.61	z	GB	FALSE	1 : -0.165	O/Sr-Ti
14.85	x	IB	FALSE	-0.038 : 1	Ti/Sr-O
15.02	y	GB	FALSE	1 : -0.014	O/Sr-Ti
15.66	z	GB	FALSE	1 : -0.464	Ti/Sr-O
15.73	y	IB	TRUE	0.223 : 1	O/Sr-Ti
15.87	x	IB	TRUE	0.48 : 1	Ti/Sr-O
16.15	y	GB	FALSE	1 : -0.382	Ti/Sr-O
16.32	y	IB	FALSE	-0.19 : 1	O/Sr-Ti
16.42	x	IB	FALSE	-0.321 : 1	O/Sr-Ti
16.64	z	GB	TRUE	1 : 0.084	Ti/Sr-O
16.90	z	IB	FALSE	-0.413 : 1	Ti/Sr-O
17.09	y	IB	FALSE	-0.74 : 1	O/Sr-Ti
17.27	x	GB	FALSE	1 : -0.052	Ti/Sr-O
17.31	y	GB	FALSE	1 : -0.793	Ti/Sr-O
17.41	x	IB	TRUE	0.393 : 1	O/Sr-Ti
17.98	y	IB	FALSE	-0.433 : 1	O/Sr-Ti
17.99	z	GB	FALSE	1 : -0.053	Ti/Sr-O
18.13	x	GB	FALSE	1 : -0.339	Ti/Sr-O
18.58	x	IB	FALSE	-0.83 : 1	O/Sr-Ti
18.69	y	IB	FALSE	-0.474 : 1	O/Sr-Ti
18.96	z	IB	FALSE	-0.715 : 1	Sr/Ti-O
19.07	z	GB	FALSE	1 : -0.91	Ti/Sr-O
19.57	z	GB	FALSE	1 : -0.415	Ti/Sr-O
19.71	x	GB	FALSE	1 : -0.353	O/Sr-Ti
19.79	z	IB	TRUE	0.167 : 1	Ti/Sr-O
19.84	x	GB	TRUE	1 : 0.018	O/Sr-Ti
19.88	z	IB	FALSE	-0.786 : 1	O/Sr-Ti
19.90	x	IB	FALSE	-0.615 : 1	O/Sr-Ti
20.21	x	IB	FALSE	-0.714 : 1	O/Sr-Ti
20.31	z	IB	FALSE	-0.547 : 1	Ti/Sr-O
20.45	x	GB	FALSE	1 : -0.234	O/Sr-Ti
20.71	y	GB	TRUE	1 : 0.531	O/Sr-Ti
20.73	z	GB	TRUE	1 : 0.225	Ti/Sr-O
21.04	x	IB	FALSE	-0.954 : 1	O/Sr-Ti

21.08	z	GB	FALSE	1 : -0.586	O/Sr-Ti
21.38	z	GB	FALSE	1 : -0.451	O/Sr-Ti
21.81	x	GB	FALSE	1 : -0.891	Sr/Ti-O
21.88	y	GB	FALSE	1 : -0.825	O/Sr-Ti
22.07	z	IB	FALSE	-0.553 : 1	O/Sr-Ti
22.30	x	IB	TRUE	0.526 : 1	O/Sr-Ti
22.46	y	GB	TRUE	1 : 0.289	Ti/Sr-O
22.60	x	IB	FALSE	-0.424 : 1	Ti/Sr-O
22.70	z	GB	TRUE	1 : 0.196	Ti/Sr-O
23.16	z	IB	FALSE	-0.013 : 1	O/Sr-Ti
23.96	x	GB	FALSE	1 : -0.83	O/Sr-Ti
24.11	z	IB	TRUE	0.534 : 1	Ti/Sr-O
24.87	x	GB	FALSE	1 : -0.71	O/Sr-Ti
25.14	z	IB	FALSE	-0.377 : 1	Ti/Sr-O
25.24	x	GB	FALSE	1 : -0.815	O/Sr-Ti
25.35	z	IB	FALSE	-0.76 : 1	O/Sr-Ti
25.60	x	IB	FALSE	-0.705 : 1	O/Sr-Ti
26.36	x	IB	FALSE	-0.524 : 1	O/Sr-Ti
26.37	x	IB	FALSE	-0.861 : 1	Sr/Ti-O

Table S4. Index of the vibrational modes in $\Sigma 5\{310\}/[001]$

Frequency (THz)	Direction	Region	Directional Agreement	"GB" : "IB"	Species
1.07	x	GB	FALSE	1 : -0.117	O/Sr-Ti
1.76	x	IB	FALSE	-0.72 : 1	Sr/Ti-O
1.86	x	IB	FALSE	-0.543 : 1	Sr/Ti-O
1.86	z	GB	TRUE	1 : 0.559	Sr/Ti-O
1.98	z	IB	FALSE	-0.523 : 1	Sr/Ti-O
2.16	z	IB	FALSE	-0.588 : 1	Sr/Ti-O
2.38	x	IB	FALSE	-0.547 : 1	Sr/Ti-O
2.46	z	GB	TRUE	1 : 0.124	Sr/Ti-O
2.61	x	IB	FALSE	-0.432 : 1	Sr/Ti-O
2.67	y	GB	FALSE	1 : -0.941	Sr/Ti-O
2.82	z	IB	FALSE	-0.907 : 1	Sr/Ti-O
2.83	y	IB	FALSE	-0.757 : 1	Sr/Ti-O
2.88	z	IB	FALSE	-0.644 : 1	O/Sr-Ti
2.89	x	IB	TRUE	0.14 : 1	Sr/Ti-O
3.01	z	GB	FALSE	1 : -0.647	Sr/Ti-O
3.20	x	GB	TRUE	1 : 0.725	O/Sr-Ti
3.23	y	IB	FALSE	-0.972 : 1	Sr/Ti-O
3.26	z	GB	FALSE	1 : -0.755	Sr/Ti-O
3.33	z	GB	FALSE	1 : -0.87	Sr/Ti-O
3.36	x	IB	FALSE	-0.46 : 1	Sr/Ti-O
3.45	y	GB	FALSE	1 : -0.991	Sr/Ti-O
3.54	y	GB	FALSE	1 : -0.883	Sr/Ti-O
3.58	x	IB	FALSE	-0.779 : 1	Sr/Ti-O
3.75	z	IB	FALSE	-0.075 : 1	O/Sr-Ti
3.76	y	GB	FALSE	1 : -0.755	Sr/Ti-O
3.78	x	IB	FALSE	-0.96 : 1	Ti/Sr-O
3.79	x	GB	FALSE	1 : -0.072	Sr/Ti-O
3.83	z	GB	FALSE	1 : -0.583	Sr/Ti-O
3.84	y	GB	FALSE	1 : -0.657	Sr/Ti-O
4.01	x	IB	FALSE	-0.918 : 1	Sr/Ti-O
4.05	z	GB	FALSE	1 : -0.618	Sr/Ti-O
4.05	y	GB	FALSE	1 : -0.622	Sr/Ti-O
4.14	z	IB	FALSE	-0.804 : 1	Sr/Ti-O
4.24	x	GB	FALSE	1 : -0.716	O/Sr-Ti
4.31	z	GB	FALSE	1 : -0.382	Sr/Ti-O
4.37	x	IB	FALSE	-0.211 : 1	Sr/Ti-O
4.40	z	GB	FALSE	1 : -0.631	Sr/Ti-O
4.43	z	GB	TRUE	1 : 0.175	Sr/Ti-O
4.47	z	GB	FALSE	1 : -0.555	Sr/Ti-O

4.48	x	IB	FALSE	-0.357 : 1	Sr/Ti-O
4.51	z	GB	FALSE	1 : -0.488	Sr/Ti-O
4.67	x	GB	FALSE	1 : -0.297	Sr/Ti-O
4.70	z	GB	FALSE	1 : -0.916	O/Sr-Ti
4.72	x	GB	FALSE	1 : -0.82	Sr/Ti-O
4.77	x	GB	FALSE	1 : -0.472	Sr/Ti-O
4.80	z	GB	FALSE	1 : -0.428	Sr/Ti-O
4.85	x	GB	TRUE	1 : 0.209	Sr/Ti-O
5.00	x	GB	FALSE	1 : -0.653	Sr/Ti-O
5.05	y	GB	FALSE	1 : -0.342	Sr/Ti-O
5.17	z	GB	FALSE	1 : -0.444	Sr/Ti-O
5.31	x	GB	FALSE	1 : -0.72	Sr/Ti-O
5.38	z	GB	FALSE	1 : -0.583	Sr/Ti-O
5.45	x	GB	FALSE	1 : -0.686	Sr/Ti-O
5.53	z	GB	TRUE	1 : 0.509	Sr/Ti-O
5.64	y	GB	TRUE	1 : 0.003	Sr/Ti-O
5.70	z	IB	TRUE	0.635 : 1	Sr/Ti-O
5.72	x	GB	FALSE	1 : -0.697	Sr/Ti-O
5.82	x	GB	TRUE	1 : 0.383	Sr/Ti-O
5.87	y	IB	FALSE	-0.169 : 1	Sr/Ti-O
5.98	x	GB	TRUE	1 : 0.605	Sr/Ti-O
6.02	z	IB	FALSE	-0.725 : 1	Sr/Ti-O
6.08	y	IB	FALSE	-0.528 : 1	Sr/Ti-O
6.11	z	IB	FALSE	-0.398 : 1	Sr/Ti-O
6.25	z	GB	FALSE	1 : -0.7	Sr/Ti-O
6.26	y	GB	FALSE	1 : -0.289	Sr/Ti-O
6.30	x	IB	FALSE	-0.447 : 1	Sr/Ti-O
6.45	x	IB	FALSE	-0.851 : 1	Ti/Sr-O
6.56	z	GB	FALSE	1 : -0.876	Ti/Sr-O
6.62	y	IB	FALSE	-0.46 : 1	Sr/Ti-O
6.66	y	GB	FALSE	1 : -0.746	Sr/Ti-O
6.70	x	IB	FALSE	-0.464 : 1	Sr/Ti-O
6.77	z	IB	FALSE	-0.613 : 1	Sr/Ti-O
6.78	y	GB	FALSE	1 : -0.615	Sr/Ti-O
6.90	z	IB	FALSE	-0.371 : 1	Sr/Ti-O
6.90	x	IB	FALSE	-0.333 : 1	Sr/Ti-O
7.12	z	IB	FALSE	-0.885 : 1	Sr/Ti-O
7.20	x	IB	FALSE	-0.73 : 1	Sr/Ti-O
7.31	z	IB	FALSE	-0.292 : 1	O/Sr-Ti
7.36	x	IB	FALSE	-0.547 : 1	Sr/Ti-O
7.38	y	GB	FALSE	1 : -0.398	Sr/Ti-O

7.61	x	IB	FALSE	-0.683 : 1	Ti/Sr-O
7.64	z	GB	FALSE	1 : -0.809	Sr/Ti-O
7.93	x	IB	FALSE	-0.881 : 1	Sr/Ti-O
8.11	z	IB	FALSE	-0.705 : 1	Sr/Ti-O
8.18	z	IB	FALSE	-0.218 : 1	Sr/Ti-O
8.26	x	GB	FALSE	1 : -0.325	O/Sr-Ti
8.27	y	IB	FALSE	-0.596 : 1	Sr/Ti-O
8.30	x	IB	FALSE	-0.697 : 1	O/Sr-Ti
8.34	z	IB	FALSE	-0.792 : 1	Ti/Sr-O
8.57	x	IB	FALSE	-0.94 : 1	Ti/Sr-O
8.62	x	GB	FALSE	1 : -0.97	Ti/Sr-O
8.72	z	IB	FALSE	-0.633 : 1	Sr/Ti-O
8.81	z	IB	FALSE	-0.872 : 1	Sr/Ti-O
9.03	z	GB	TRUE	1 : 0.218	O/Sr-Ti
9.16	x	IB	FALSE	-0.812 : 1	Ti/Sr-O
9.18	x	GB	FALSE	1 : -0.911	Ti/Sr-O
9.21	z	GB	FALSE	1 : -0.576	O/Sr-Ti
9.44	x	GB	FALSE	1 : -0.432	Sr/Ti-O
9.46	z	IB	TRUE	0.39 : 1	Sr/Ti-O
9.72	z	IB	FALSE	-0.887 : 1	Sr/Ti-O
9.79	x	IB	FALSE	-0.555 : 1	Ti/Sr-O
9.86	z	GB	FALSE	1 : -0.623	O/Sr-Ti
9.98	x	IB	TRUE	0.268 : 1	Ti/Sr-O
10.03	x	GB	TRUE	1 : 0.017	O/Sr-Ti
10.20	z	GB	FALSE	1 : -0.76	Ti/Sr-O
10.26	x	IB	TRUE	0.606 : 1	Ti/Sr-O
10.28	x	IB	FALSE	-0.806 : 1	Ti/Sr-O
10.32	z	IB	FALSE	-0.654 : 1	O/Sr-Ti
10.42	x	GB	FALSE	1 : -0.098	O/Sr-Ti
10.57	z	IB	FALSE	-0.695 : 1	Sr/Ti-O
10.70	x	IB	FALSE	-0.557 : 1	Ti/Sr-O
10.78	x	GB	FALSE	1 : -0.829	Ti/Sr-O
10.87	z	GB	TRUE	1 : 0.776	O/Sr-Ti
10.93	x	GB	FALSE	1 : -0.347	O/Sr-Ti
11.02	z	IB	FALSE	-0.353 : 1	Sr/Ti-O
11.05	y	GB	FALSE	1 : -0.697	O/Sr-Ti
11.22	z	GB	FALSE	1 : -0.499	O/Sr-Ti
11.27	y	GB	FALSE	1 : -0.683	Sr/Ti-O
11.49	x	IB	TRUE	0.387 : 1	Ti/Sr-O
11.51	z	IB	FALSE	-0.885 : 1	Ti/Sr-O
11.62	y	GB	FALSE	1 : -0.839	O/Sr-Ti

11.72	y	IB	FALSE	-0.179 : 1	O/Sr-Ti
11.97	y	GB	FALSE	1 : -0.842	Sr/Ti-O
12.11	z	GB	FALSE	1 : -0.598	O/Sr-Ti
12.18	y	IB	FALSE	-0.828 : 1	Ti/Sr-O
12.31	y	GB	FALSE	1 : -0.96	Ti/Sr-O
12.33	z	GB	FALSE	1 : -0.693	Ti/Sr-O
12.44	x	GB	FALSE	1 : -0.379	O/Sr-Ti
12.46	y	IB	FALSE	-0.923 : 1	Sr/Ti-O
12.58	x	GB	FALSE	1 : -0.625	O/Sr-Ti
12.63	y	GB	FALSE	1 : -0.496	Sr/Ti-O
12.73	x	GB	FALSE	1 : -0.363	O/Sr-Ti
12.73	y	GB	FALSE	1 : -0.181	O/Sr-Ti
12.76	y	IB	TRUE	0.652 : 1	Ti/Sr-O
12.78	x	IB	FALSE	-0.058 : 1	O/Sr-Ti
12.79	z	GB	FALSE	1 : -0.441	O/Sr-Ti
12.99	y	GB	FALSE	1 : -0.283	O/Sr-Ti
13.15	y	GB	FALSE	1 : -0.807	Sr/Ti-O
13.24	y	IB	TRUE	0.176 : 1	O/Sr-Ti
13.31	z	IB	TRUE	0.273 : 1	Ti/Sr-O
13.32	x	GB	FALSE	1 : -0.786	Ti/Sr-O
13.39	z	IB	TRUE	0.11 : 1	O/Sr-Ti
13.43	x	IB	FALSE	-0.02 : 1	O/Sr-Ti
13.52	y	IB	TRUE	0.541 : 1	Ti/Sr-O
13.64	z	GB	FALSE	1 : -0.746	Ti/Sr-O
13.71	x	IB	TRUE	0.795 : 1	O/Sr-Ti
13.78	y	GB	FALSE	1 : -0.61	O/Sr-Ti
13.81	z	GB	FALSE	1 : -0.504	O/Sr-Ti
13.84	x	IB	TRUE	0.133 : 1	O/Sr-Ti
13.86	y	GB	FALSE	1 : -0.948	Sr/Ti-O
13.93	z	IB	TRUE	0.447 : 1	O/Sr-Ti
13.97	x	GB	TRUE	1 : 0.044	O/Sr-Ti
13.99	z	IB	FALSE	-0.062 : 1	O/Sr-Ti
14.05	y	IB	FALSE	-0.896 : 1	O/Sr-Ti
14.12	z	GB	FALSE	1 : -0.874	O/Sr-Ti
14.15	x	GB	TRUE	1 : 0.776	Ti/Sr-O
14.17	x	IB	TRUE	0.951 : 1	Ti/Sr-O
14.19	z	GB	FALSE	1 : -0.142	O/Sr-Ti
14.30	y	IB	TRUE	0.046 : 1	Ti/Sr-O
14.39	x	IB	FALSE	-0.716 : 1	Ti/Sr-O
14.46	y	IB	TRUE	0.843 : 1	O/Sr-Ti
14.48	z	GB	TRUE	1 : 0.346	O/Sr-Ti

14.60	x	GB	TRUE	1 : 0.577	Ti/Sr-O
14.64	z	GB	TRUE	1 : 0.214	O/Sr-Ti
14.82	x	GB	TRUE	1 : 0.507	O/Sr-Ti
15.13	z	GB	FALSE	1 : -0.63	O/Sr-Ti
15.60	z	IB	TRUE	0.277 : 1	O/Sr-Ti
15.68	x	IB	TRUE	0.303 : 1	O/Sr-Ti
15.76	x	IB	TRUE	0.404 : 1	Ti/Sr-O
16.13	z	GB	TRUE	1 : 0.319	O/Sr-Ti
16.14	x	IB	FALSE	-0.603 : 1	O/Sr-Ti
16.35	z	GB	FALSE	1 : -0.203	Ti/Sr-O
16.46	x	IB	FALSE	-0.195 : 1	O/Sr-Ti
16.68	x	GB	FALSE	1 : -0.374	Sr/Ti-O
16.83	z	IB	TRUE	0.021 : 1	O/Sr-Ti
17.20	z	GB	TRUE	1 : 0.132	O/Sr-Ti
17.25	x	IB	FALSE	-0.564 : 1	Ti/Sr-O
17.83	x	IB	FALSE	-0.621 : 1	O/Sr-Ti
17.96	z	GB	FALSE	1 : -0.605	O/Sr-Ti
18.42	z	GB	FALSE	1 : -0.299	O/Sr-Ti
18.64	x	IB	FALSE	-0.949 : 1	Ti/Sr-O
18.99	x	IB	FALSE	-0.316 : 1	O/Sr-Ti
19.00	z	IB	TRUE	0.301 : 1	O/Sr-Ti
19.16	z	GB	FALSE	1 : -0.652	Ti/Sr-O
19.32	x	IB	FALSE	-0.769 : 1	Ti/Sr-O
19.41	z	IB	FALSE	-0.28 : 1	Ti/Sr-O
19.42	x	GB	FALSE	1 : -0.719	O/Sr-Ti
19.64	z	IB	TRUE	0.87 : 1	Ti/Sr-O
19.68	x	GB	FALSE	1 : -0.768	Ti/Sr-O
19.84	x	GB	FALSE	1 : -0.893	Ti/Sr-O
20.01	z	IB	FALSE	-0.719 : 1	Ti/Sr-O
20.11	y	IB	TRUE	0.328 : 1	Ti/Sr-O
20.11	x	IB	FALSE	-0.718 : 1	Ti/Sr-O
20.15	z	GB	FALSE	1 : -0.767	O/Sr-Ti
20.28	x	IB	FALSE	-0.953 : 1	Ti/Sr-O
20.31	z	IB	FALSE	-0.9 : 1	Ti/Sr-O
20.68	z	GB	FALSE	1 : -0.416	O/Sr-Ti
20.79	z	IB	FALSE	-0.112 : 1	O/Sr-Ti
20.84	x	IB	FALSE	-0.774 : 1	O/Sr-Ti
21.00	x	IB	FALSE	-0.685 : 1	O/Sr-Ti
21.04	z	IB	FALSE	-0.926 : 1	Sr/Ti-O
21.06	x	IB	FALSE	-0.928 : 1	Ti/Sr-O
21.09	x	IB	FALSE	-0.938 : 1	O/Sr-Ti

21.11	y	GB	FALSE	1 : -0.758	Ti/Sr-O
21.17	z	GB	FALSE	1 : -0.818	Sr/Ti-O
21.25	z	GB	FALSE	1 : -0.739	O/Sr-Ti
21.38	y	GB	FALSE	1 : -0.657	Ti/Sr-O
21.41	z	IB	FALSE	-0.742 : 1	O/Sr-Ti
21.50	z	IB	FALSE	-0.831 : 1	O/Sr-Ti
21.67	z	IB	FALSE	-0.897 : 1	Ti/Sr-O
21.68	x	GB	FALSE	1 : -0.871	O/Sr-Ti
21.77	x	GB	FALSE	1 : -0.858	Ti/Sr-O
21.86	z	GB	FALSE	1 : -0.842	O/Sr-Ti
22.02	y	IB	FALSE	-0.966 : 1	Ti/Sr-O
22.09	y	GB	TRUE	1 : 0.432	O/Sr-Ti
22.13	y	GB	FALSE	1 : -0.878	Ti/Sr-O
22.32	y	GB	FALSE	1 : -0.939	O/Sr-Ti
22.48	x	IB	FALSE	-0.216 : 1	Ti/Sr-O
22.49	z	GB	FALSE	1 : -0.292	Ti/Sr-O
22.77	x	IB	TRUE	0.441 : 1	Ti/Sr-O
22.78	y	IB	FALSE	-0.007 : 1	Ti/Sr-O
23.04	z	GB	FALSE	1 : -0.633	O/Sr-Ti
23.29	x	IB	FALSE	-0.84 : 1	Ti/Sr-O
23.40	z	GB	TRUE	1 : 0.012	Ti/Sr-O
23.65	x	IB	FALSE	-0.744 : 1	Ti/Sr-O
23.78	z	GB	FALSE	1 : -0.388	O/Sr-Ti
24.42	z	GB	FALSE	1 : -0.608	Ti/Sr-O
24.45	x	IB	FALSE	-0.688 : 1	Ti/Sr-O
24.86	z	IB	FALSE	-0.414 : 1	Ti/Sr-O
24.93	x	GB	FALSE	1 : -0.824	O/Sr-Ti
25.14	z	IB	FALSE	-0.607 : 1	Ti/Sr-O
26.21	x	GB	FALSE	1 : -0.451	Ti/Sr-O
26.31	z	IB	FALSE	-0.734 : 1	Ti/Sr-O
26.96	x	IB	FALSE	-0.918 : 1	O/Sr-Ti
26.97	z	GB	FALSE	1 : -0.255	Ti/Sr-O
28.50	x	GB	FALSE	1 : -0.504	Ti/Sr-O

Section S3. Thermal conductivity of layered nanostructures – the directional components

Figure S4 presents the in-plane (\parallel) and the out-of-plane (\perp) thermal conductivities for all the layered nanostructures studied. The in-plane (\parallel) thermal conductivity corresponds to the average thermal conductivity calculated in the Y (i.e. the direction of the grain boundary pipe) and Z directions of the simulation cells, thus parallel to the grain boundary plane. The out-of-plane (\perp) thermal conductivity corresponds to the contribution calculated across (i.e. perpendicular to) the grain boundary plane, which is the X direction in the simulation cells.

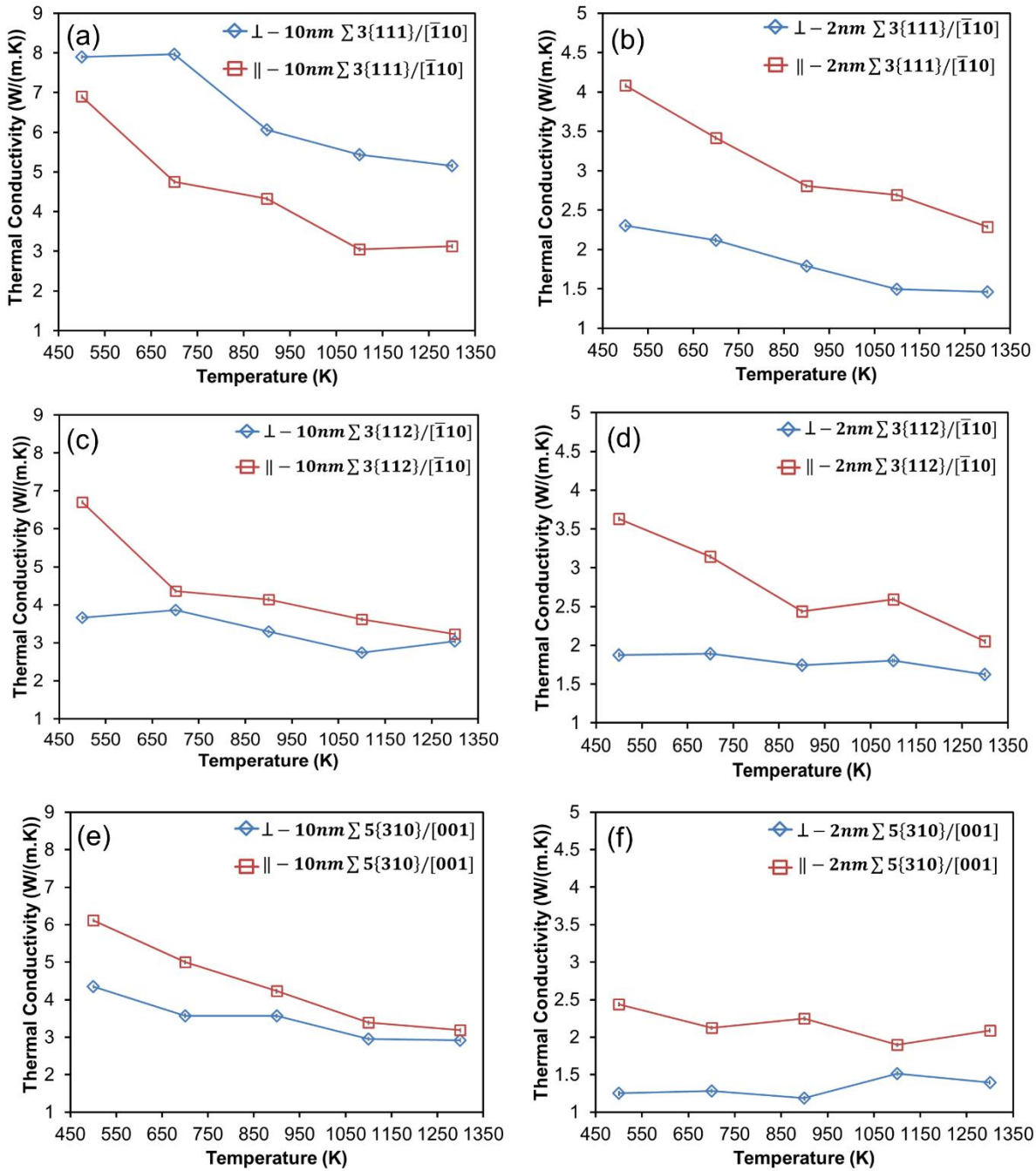


Figure S4. In-plane (\parallel) and out-of-plane (\perp) components of the thermal conductivity for 10nm-GB (a) $\Sigma 3\{111\}/[\bar{1}10]$, (c) $\Sigma 3\{112\}/[\bar{1}10]$ and (e) $\Sigma 5\{310\}/[001]$ and 2nm-GB (b) $\Sigma 3\{111\}/[\bar{1}10]$, (d) $\Sigma 3\{112\}/[\bar{1}10]$ and (f) $\Sigma 5\{310\}/[001]$.

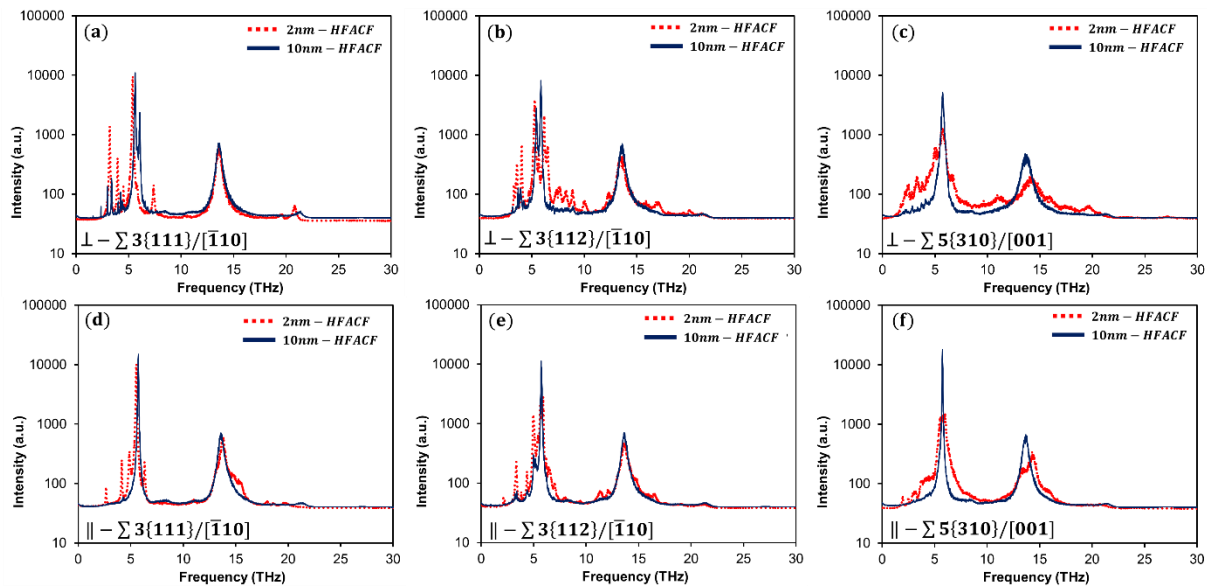


Figure S5. The heat-flux autocorrelation functions (HFACF) spectra at 500 K for 2nm-GB and 10nm-GB $\Sigma 3\{111\}/[\bar{1}\bar{1}0]$, $\Sigma 3\{112\}/[\bar{1}\bar{1}0]$ and $\Sigma 5\{310\}/[001]$ grain boundary. The in-plane (\parallel) and out-of-plane (\perp) components are separated for each grain boundary. The intensities are in arbitrary units - Log₁₀ scale.

References

- 1 M. S. Green, *J. Chem. Phys.*, 1954, **22**, 398-413.
- 2 R. Kubo, *J. Phys. Soc. Jpn.*, 1957, **12**, 570-586.
- 3 S. Plimpton, *J. Comput. Phys.*, 1995, **117**, 1-19.
- 4 T.W. Sirk, S. Moore and E.F. Brown, *J. Chem. Phys.*, 2013, **138**, 064505.
- 5 P. K. Schelling, S. R. Phillpot and P. Kebinski, *Phys. Rev. B*, 2002, **65**, 144306.
- 6 A. J. H. McGaughey and J. M. Larkin, *Ann. Rev. Heat Transfer*, 2014, **17**, 49-87.
- 7 A. J. H. McGaughey and M. Kaviani, *Int. J. Heat Mass Transfer*, 2004, **47**, 1799-1816.
- 8 M. T. Dove, *Structure and Dynamics: An Atomic View of Materials*, Oxford University Press, Oxford, 2003.
- 9 S. R. Yeandel, M. Molinari and S. C. Parker, *RSC Adv.*, 2016, **6**, 114069-114077.
- 10 J. D. Gale and A. L. Rohl, *Mol. Simulat.*, 2003, **29**, 291-341.
- 11 P. Canepa, PhD Thesis, University of Kent, 2012.
- 12 N. R. Williams, M. Molinari, S. C. Parker and M. T. Storr, *J. Nucl. Mater.*, 2015, **458**, 45-55.
- 13 G. W. Watson, E. T. Kelsey, N. H. deLeeuw, D. J. Harris and S. C. Parker, *J. Chem. Soc., Faraday Trans.*, 1996, **92**, 433-438.
- 14 A. Togo, F. Oba and I. Tanaka, *Phys. Rev. B*, 2008, **78**, 134106.
- 15 J. M. Skelton, S. C. Parker, A. Togo, I. Tanaka and A. Walsh, *Phys. Rev. B*, 2014, **89**.
- 16 A. Togo, L. Chaput and I. Tanaka, *Phys. Rev. B*, 2015, **91**, 094306.
- 17 E. S. Landry, M. I. Hussein and A. J. H. McGaughey, *Phys. Rev. B*, 2008, **77**, 184302.